Nanoscale

PAPER

View Article Online
View Journal | View Issue

Cite this: *Nanoscale*, 2019, **11**, 2299

Dynamics of amphiphilic block copolymers in an aqueous solution: direct imaging of micelle formation and nanoparticle encapsulation†

Chang Li,[a,b,c] Che Chen Tho,[a,b,d] Daria Galaktionova,[e] Xin Chen,[c] Petr Král[e,f] and Utkur Mirsaidov[*a,b,d,g,h]

Received 5th November 2018,
Accepted 2nd January 2019

DOI: 10.1039/c8nr08922a

rsc.li/nanoscale

Micelles formed through the aggregation of amphiphilic block copolymers are ideal drug nanocarriers. Despite their importance in nanomedicine, the detailed mechanisms through which micelles form and copolymers encapsulate the target nanomaterials are unclear. Here, using *in situ* liquid cell transmission electron microscopy imaging, we capture both the dynamics of micelle formation and their encapsulation of gold nanoparticles (NPs) in an aqueous solution. Our observations reveal that the amphiphilic block copolymers aggregate and rearrange to form a micelle with a hydrophobic and rigid core, surrounded by a corona of hydrophilic blocks that extend into the solution. These micelles are stable against coalescence, and once mature, they do not merge. We also show that the encapsulation of hydrophobic NPs is a self-limiting process, which occurs through gradual adsorption of block copolymers; the growth of a polymeric shell around the NPs, shielding them from water, ceases when the NPs are fully covered by the adsorbed copolymers. The insights from these observations are of fundamental importance for the design of biocompatible soft materials.

Introduction

Self-assembly of amphiphilic molecules with hydrophilic heads and hydrophobic tails plays an important role in many natural and industrial processes.[1–3] For example, in living species, cellular membranes and vesicles form from phospholipids, small molecules that consist of two hydrophobic fatty acid tails and a hydrophilic head (polar phosphate group).[4–7] Molecular assemblies formed from amphiphilic block copolymers usually have better stability and durability than those formed by phospholipids or small surfactants, which makes them attractive for drug delivery,[8,9] nanoscale patterning,[10] and as templates for nanomaterial synthesis[11,12] and catalysis.[13,14] Typically, the amphiphilic block copolymers are formed by covalently bonded hydrophobic and hydrophilic blocks with one or more groups of the same kind.[15] In a solvent, amphiphilic block copolymers with soluble and insoluble blocks can self-assemble into micelles with various shapes and sizes.[15,16] In a given solvent, the micelles form above a critical micelle concentration (CMC) or critical micelle temperature (CMT) of the copolymers, where the insoluble blocks aggregate into dense micellar cores surrounded by coronas formed from the soluble blocks extending into the solvent.[17] Micelles formed by amphiphilic block copolymers can be used to encapsulate NPs and drugs in order to enhance their solubility[18] and stability,[19] and reduce their toxicity,[6] which makes the micelles an ideal candidate for bioimaging[20,21] and biomedical[22,23] applications.

Even though terminal structures of micelles are known, detailed mechanisms of their formation are less clear. For example, the individual stages of the core–corona formation during the micelle growth and cargo encapsulation by block copolymers are largely unknown. This gap in our understandings of micelle formation or cargo encapsulation mainly stems from the lack of suitable methods that enable direct time-dependent observations of these nanoscale processes in a solution. Current characterization techniques based on indirect

[a]*Department of Physics, National University of Singapore, 117551, Singapore. E-mail: mirsaidov@nus.edu.sg*
[b]*Centre for BioImaging Sciences and Department of Biological Sciences, National University of Singapore, 117557, Singapore*
[c]*School of Materials Science and Engineering, East China University of Science and Technology, Shanghai 200237, P. R. China*
[d]*Centre for Advanced 2D Materials and Graphene Research Centre, National University of Singapore, 117546, Singapore*
[e]*Department of Chemistry, University of Illinois at Chicago, Chicago, IL 60607, USA*
[f]*Departments of Physics and Biopharmaceutical Sciences, University of Illinois at Chicago, Chicago, IL 60607, USA*
[g]*NUSNNI-NanoCore, National University of Singapore, 117411, Singapore*
[h]*Department of Materials Science and Engineering, National University of Singapore, 117575, Singapore*

†Electronic supplementary information (ESI) available. See DOI: 10.1039/c8nr08922a

methods such as dynamic light scattering,[24,25] small angle neutron scattering,[26–28] and differential scanning calorimetry[29,30] provide useful insights into micelle formation by tracking the time-dependent distribution of micelle size, shape, CMC, and CMT. However, these approaches do not reveal the detailed stages of individual micelle evolution, for which direct time-resolved imaging of micelle formation aided with molecular-scale simulations is needed.

In situ liquid phase transmission electron microscopy (TEM) enables real-time imaging of individual nanoscale events in a solution.[31–33] This approach has been crucial in revealing different nucleation and growth modes of metallic NPs,[34,35] NP self-assembly,[36,37] and dynamics of organic polymers[38] in a solution. Most notably, recent dynamic studies by Gianneschi *et al.* revealed the growth of micelles through fusion[39] and polymerization of diblock copolymers.[40] Here, using *in situ* liquid cell TEM imaging combined with atomistic molecular dynamics (MD) simulations, we describe the dynamics of triblock copolymer micelle formation, their interactions, and their encapsulation of NPs.

Results and discussion

To explore the dynamics of micelle formation in water, we use an aqueous solution of (ethylene oxide)$_{100}$-*block*-(propylene oxide)$_{65}$-*block*-(ethylene oxide)$_{100}$, (EO_{100}-PO_{65}-EO_{100}) (fully extended length of ~80 nm). We chose EO_{100}-PO_{65}-EO_{100} because it is a very common and commercially available amphiphilic triblock copolymer (Pluronic F127).[41] Here, poly(ethylene oxide) and poly(propylene oxide) blocks are hydrophilic and hydrophobic blocks of the copolymer, respectively.[42]

The formation dynamics of spherical micelles from EO_{100}-PO_{65}-EO_{100} copolymers, as captured using *in situ* liquid-phase TEM, is shown in Fig. 1A (ESI Movie 1†). The micelles nucleated and grew in an aqueous copolymer solution at a concentration of 7.5 mg mL^{-1}, which is well above their CMC (~1 mg mL^{-1}).[43] Nucleation of micelles and their subsequent growth occurs readily; the micelles grew rapidly until their diameter reached 8–15 nm, at which point their growth slowed down and ceased (Fig. 1B). The initial phase (t = 0–20 s) of micelle formation in water was marked with a rapid increase in their total number in the field of view (Fig. 1C). Later, due to the depletion of copolymers in the solution (reaching CMC), the nucleation rate of micelles reduced gradually (t > 20 s). Note that because of the delay (~5 min) associated with loading of freshly prepared copolymer solution and subsequent imaging, there were some micelles already present in the solution at t = 0 s. To minimize the beam induced damage, time-series of *in situ* TEM images were recorded with low electron flux of <4.5 e$^-$ (Å^2 s)$^{-1}$.

For the triblock copolymer molecules, EO_{100}-PO_{65}-EO_{100}, dissolved in water, we expect the micelle core to be comprised of hydrophobic blocks (PO_{65}) surrounded by a corona from hydrophilic blocks (EO_{100}). To understand in details the dynamics of

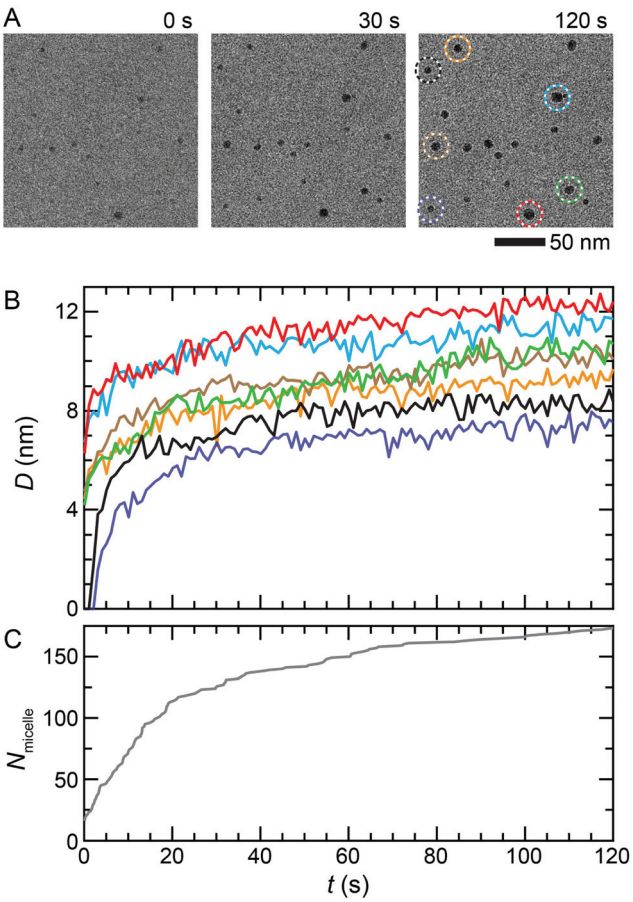

Fig. 1 Dynamics of micelle formation. (A) A time series of *in situ* TEM images showing the nucleation and growth of micelles from an aqueous solution of amphiphilic triblock copolymers (EO_{100}-PO_{65}-EO_{100}) (ESI Movie 1†). (B) The micelle diameters as a function of time. Different colors correspond to different micelles indicated by dashed circles in the panel (A). (C) The total number of micelles as a function of time.

micelle formation, we tracked the growth of individual micelles. The triblock copolymers form aggregates that grew with time (Fig. 2A: t < 80 s, Fig. 2B: t < 10 s) as more copolymer molecules join the formed molecular cluster (ESI Movie 2 and 3†). The overall contrast of these spherical aggregates throughout the early stages of the growth remained uniform. Later, a subtle spherical region with a dark contrast appeared near the center of the aggregates (Fig. 2A: t = 80 s, Fig. 2B: t = 10 s) and remained detectable during the rest of the growth (Fig. 2A: t > 80 s, Fig. 2B: t > 10 s). We attribute this change of the image contrast to a gradual rearrangement of the block copolymers within the aggregate into a micelle with a dense hydrophobic core (dark contrast region) surrounded by the solvated corona (lighter contrast region) (also see ESI Section S1†). In a few occasions during our observations, the central regions with weak dark contrast intermittently disappeared before reappearing again (ESI Movie 2†). While we do not have a clear explanation for this intermittent change of the contrast, we suspect it to be due to a slight change in the core density or transient crystallization of the otherwise glassy core during the

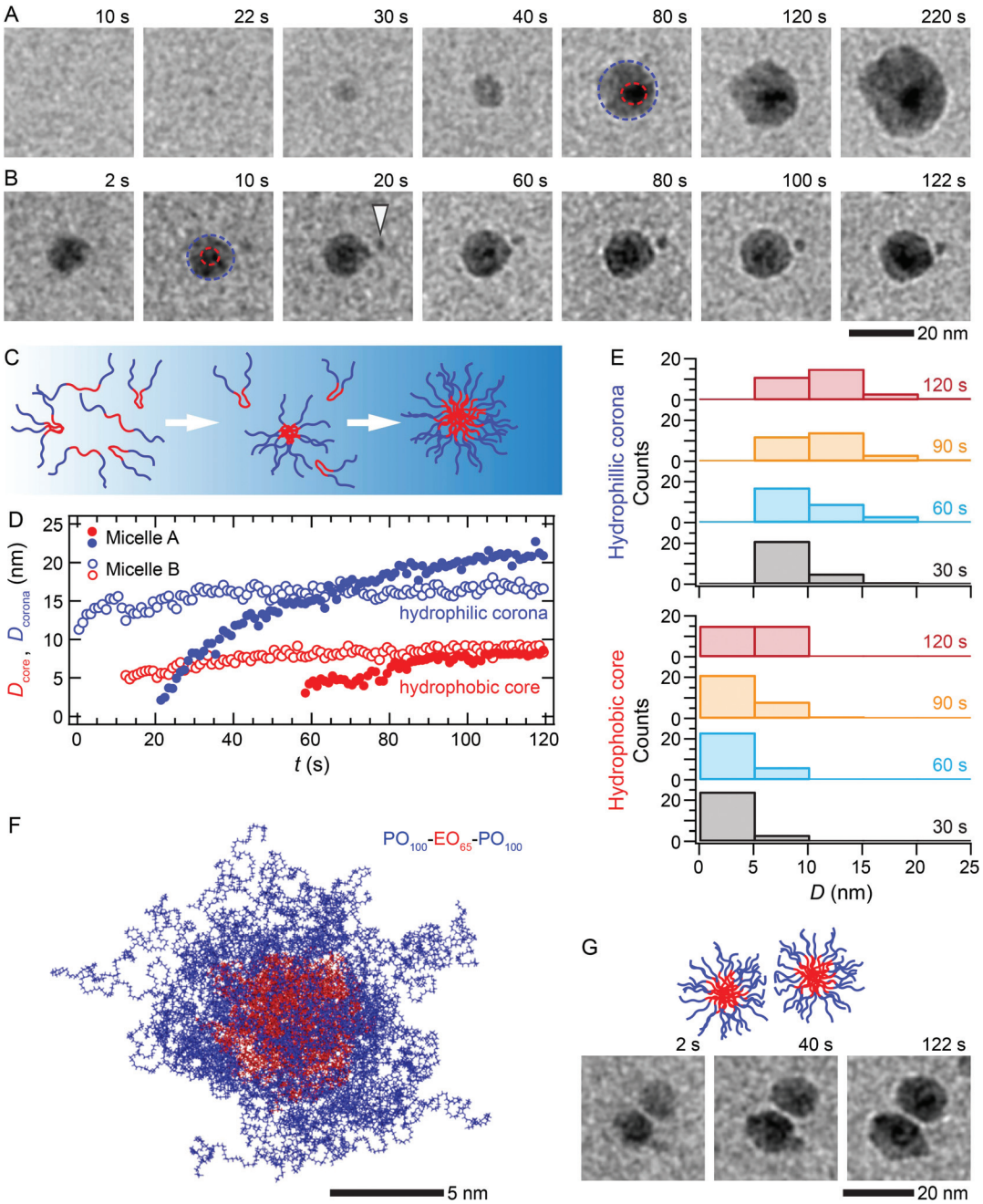

Fig. 2 Formation of micelles from the triblock copolymers. (A, B) Time series of *in situ* TEM images showing the formation of two micelles in copolymer (EO_{100}-PO_{65}-EO_{100}) solution (ESI Movies 2 and 3†). White arrow at t = 20 s in panel (B) indicates a small copolymer aggregate that comes into contact with the larger micelle. (C) Schematic of the micelle formation process. (D) Diameters of the core (red) and corona (blue) of the micelles shown in (A) (solid circles) and (B) (open circles) as a function of time. Core contrast is weak and detectable only after sometime when the large enough (>10 nm) copolymer aggregates form. (E) Distribution of corona (top) and core (bottom) diameters at different time points (~30 s, ~60 s, ~90 s, and ~120 s) for 30 micelles. To enhance the contrast between corona and core, a Gaussian blurring with σ = 2 pixels was applied to TEM mages in panels (A), (B), and (E). (F) A snapshot of MD simulation of a micelle formed from 20 triblock copolymer molecules (ESI Movie 4†). Water molecules are omitted for clarity. (G) Interaction between two mature micelles displaying the absence of a post-contact coalescence.

micelle growth. Schematic shown in Fig. 2C describes the proposed process of micelle formation where the expected coiling of hydrophobic blocks occurs in the solution, and the subsequent assembly into a micelle is driven by hydrophobic interactions between these coiled PO_{65} blocks. The overall micelle size reaches 10–20 nm, whereas the core diameter is <10 nm (Fig. 2D). To identify the number of polymers in the micelles, we characterized the evolution of 30 micelles and found the diameter of their core and corona to be 4–9 nm and 8–15 nm, respectively (Fig. 2E).

To understand better the structure of these micelles, we simulated them by atomistic MD simulations.[44] Fig. 2F shows the simulated micelle consisting of 20 triblock copolymers (EO_{100}-PO_{65}-EO_{100}) used in the experiments. The diameters of the core and corona are ~7 nm and ~15 nm, respectively, and it is consistent with our experimentally observed sizes (Fig. 2E). Micelles formed from 10, 20, and 40 copolymers are compared in ESI Section 2.† The simulations also reveal that the hydrophobic core of these micelles is very rigid compared to the outer solvated and floppy corona (ESI Movie 4†).

Our observations suggest that these micelles grow mainly *via* a gradual attachment of copolymer molecules, and to a lesser extent, by coalescence of smaller micelles. For example, when a small copolymer aggregate contacts a larger (mature) micelle, they rarely coalesce and remain well-separated (Fig. 2B: $t \geq 20$ s). In our experiments, we observed the formation of 174 micelles in total, nineteen of which come into contact. From this nineteen micelles, only two mature micelles coalesced with other two small polymeric aggregates (ESI Section S3†). The absence of coalescence is even more drastic when the micelle-micelle contact is between two bigger (mature) micelles. Despite the direct contact, micelles remain well separated and do not coalesce within the observation timescales (Fig. 2G). Note that the coalescence can occur through the fusion of micelles and dynamic exchange of copolymers between the micelles.[45,46] In both cases, the coalescence is a rapid process and occurs readily only for so-called *dynamic* micelles comprising of smaller (<4 nm) amphiphilic molecules.[45] Recently, this process has been directly observed by *in situ* TEM.[39] However, for polymeric micelles with large

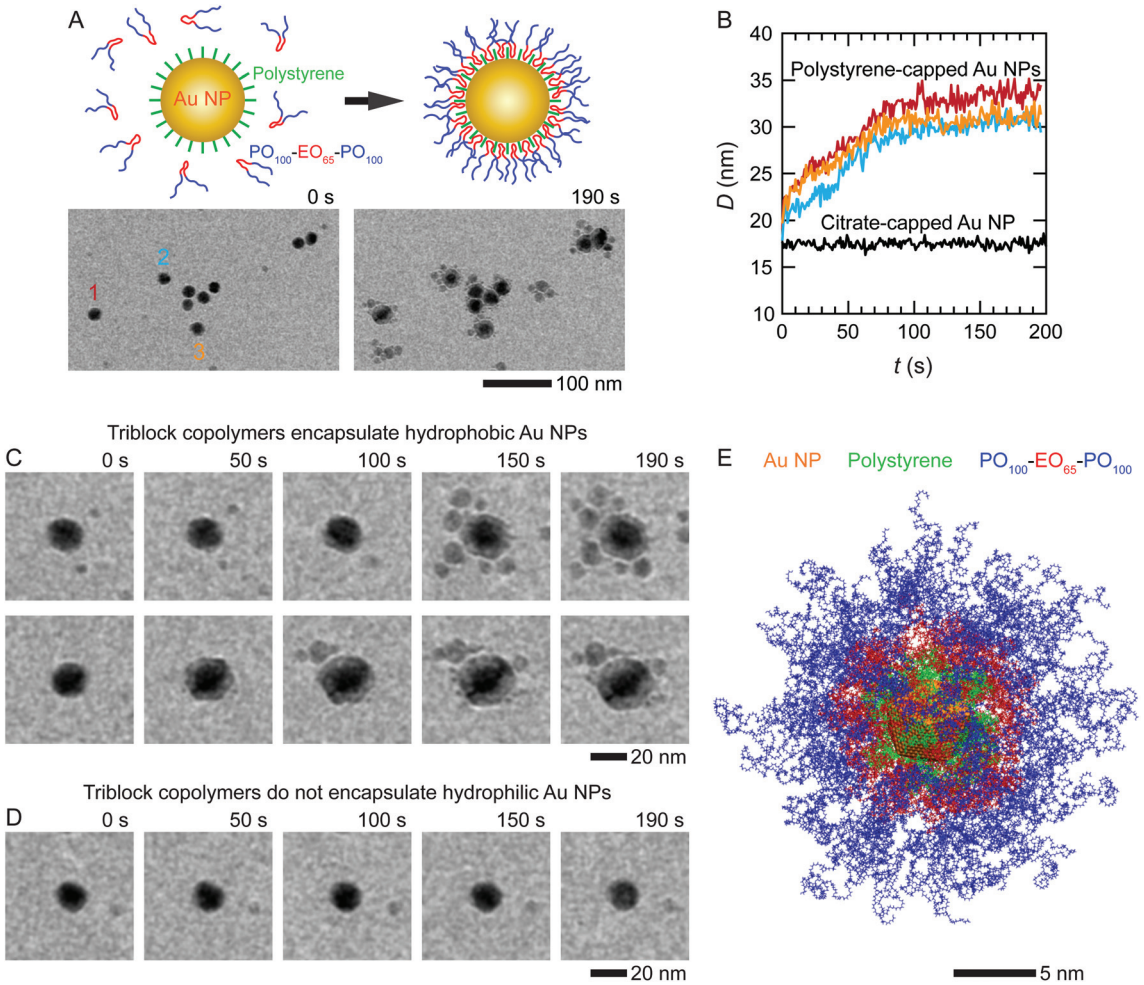

Fig. 3 Encapsulation of gold NPs with the triblock copolymers. (A) Polystyrene-capped (hydrophobic) ~18 nm gold NPs in an aqueous solution of copolymer (EO_{100}-PO_{65}-EO_{100}) at t = 0 s and t = 190 s (ESI Movie 5†). The image at t = 190 s shows that the NPs are fully encapsulated by copolymers. (B) The outer diameters of three NPs shown in (A) (polystyrene-capped) and one NP shown in (D) (citrate-capped) as a function of time. (C) Time series of *in situ* TEM images showing the encapsulation process. In addition to the NP encapsulation, other micelles also form in the solution and cluster around the NP. Note that micelles in this solution form not only near the NPs but also away from them as seen in (A) and ESI Movie 5† (*i.e.*, micelle nucleation is not necessarily triggered by NPs). (D) In the case of gold NPs capped with citrate (hydrophilic), no encapsulation by copolymers is observed. Note that small micelles still from in solution away from the NP. The electron beam flux used for imaging is 1.4 e^{-} ($Å^2$ s)$^{-1}$. (E) MD simulation showing the encapsulation of polystyrene-coated gold NP, whose diameter is 5.2 nm, with 40 molecules of EO_{100}-PO_{65}-EO_{100} (ESI Movie 6†). Water molecules are omitted for clarity.

copolymers, timescale for the fusion is very long, and micelles are kinetically frozen[47–50] with the exception of few cases.[46] Moreover, the exchange rate of copolymers between such frozen micelles is also very low because both the exit and insertion rates of copolymers decrease drastically with the increase in the length of hydrophobic PO_n blocks.[51] The reason for this reduction in copolymer mobility and increased micelle stability is the entanglement of hydrophobic blocks within the core.[45] The stability of block copolymer micelles makes them appealing for drug delivery applications where long circulation times prior to drug release are required.[52]

The key advantage of amphiphilic block copolymers is that they can readily adsorb onto hydrophobic surfaces, thereby providing effective encapsulation for a potential hydrophobic cargo, such as NPs, which increases the solubility of otherwise insoluble NPs or drugs.[15,18,21,53] To visualize the dynamics of the NP encapsulation, we mixed an aqueous suspension of polystyrene-capped hydrophobic gold NPs with the block copolymers at a concentration of 7.5 mg mL^{-1}. Inside the solution, copolymers slowly form a shell encapsulating the NPs until the visible shell thickness reaches ~10 nm, at which point the shell growth ceases (Fig. 3A–C) (ESI Movie 5†). A copolymer shell of a similar thickness was also observed in our *ex situ* experiments (ESI Section S4†). Here, the linear length of a copolymer chain is ~80 nm, but the copolymer shell thickness is only ~10 nm (Fig. 3C), which suggests that when coiled hydrophobic blocks adsorb to the NP, hydrophilic blocks are folded and aggregated. Note that the difference between the encapsulation of the hydrophobic NPs is different from the micelles formation; micelles form because of the hydrophobic interaction between the copolymers whereas the encapsulation is due to the hydrophobic interaction between the NP and the copolymer.

The NP encapsulation by copolymers is a self-limiting process. Note that few micelles are also forming nearby the NPs (Fig. 3C). These micelles formed and grew even after the growth of the encapsulating shell of NPs ceased at $t \approx 90$ s (Fig. 3B), which suggests that the cessation of the growth of the polymeric shell around the NPs is not due to the depletion of the copolymers in the solution. The growth of polymeric shells cease because adsorbed copolymers fully cover the hydrophobic surface of the NPs, leaving no space for further copolymer adsorption as validated by our MD simulation. Fig. 3E shows the MD simulated polystyrene-capped gold NP encapsulated by 40 block copolymer molecules, forming ~10 nm-thick polymeric shell (ESI Movie 6†). Here, hydrophobic blocks are adsorbed on the NP due to strong hydrophobic interaction between the polystyrene and EO_{65}-block of the copolymer (ESI Section S2†). To verify experimentally that the NP encapsulation by copolymers is distinctly due to the hydrophobicity of the (polystyrene-capped) NPs, we repeated the same experiment with hydrophilic (citrate-capped) gold NPs. In this case, we did not observe the encapsulation both in our *in situ* (Fig. 3D) and *ex situ* experiments (Fig. S6†).

The micelle nucleation and growth around the NPs (Fig. 3A and C) suggests that the copolymers accumulate near the NPs because of their hydrophobic attraction to the NPs. Moreover, these micelles come into direct contact with the copolymer-encapsulated gold NPs but remain well-separated. The absence of the micelle–NP, NP–NP, and micelle–micelle coalescence again suggests that not only the micelles but also copolymers on the NPs are kinetically frozen within the experimental timescales.

Conclusion

The observed dynamics of core and corona evolution during the formation of polymeric micelles raises a number of interesting questions. First, does the hydrophobic core start to form at the onset of copolymer aggregation or does it form by the rearrangement of copolymers after the aggregation? Second, will the formation dynamics for polymorphic micelles be the same (*i.e.*, grow *via* the attachment of individual copolymers) or will they assemble from smaller individual spherical micelles? Finally, the *in situ* TEM-based approach to observing the encapsulation of gold NPs directly can be extended to study the controlled release of polymer-encapsulated NPs under different physiological conditions. The insight into the details of NP release processes using this approach can be a powerful technique to screen different polymers for drug delivery applications.

Methods

Materials

The following reagents were used to prepare the aqueous solution of micelles and NPs: Pluronic F127 (EO_{100}-PO_{65}-EO_{100}, M_w = 12 600 g mol^{-1}, Cat. No.: P2443, Sigma-Aldrich Co., St Louis, MO, USA), 10–15 nm polystyrene-capped gold NPs in chloroform (0.375%, (w/v)) (Cat. No.: E11-10-PS-CHL-2.5-0.25, Nanopartz Co., Loveland, CO, USA), 15 nm citrate-capped gold NPs (Cat. No.: 777137, Sigma-Aldrich Co., St Louis, MO, USA.), chloroform ($CHCl_3$, Cat. No.: C/4960/17, Fisher Scientific UK Ltd, Leicestershire, LE11 5RG, UK). All chemicals were used as received without further purification. Deionized water with the resistivity of 18.2 MΩ cm was used to prepare all the dilutions of block copolymers and NPs.

Experimental procedures

For micelle formation experiments described in the text, ~0.6 μL aqueous solution of Pluronic F-127 at a concentration of ~7.5 mg mL^{-1} was loaded into our custom microfabricated liquid cell with two ~20 nm thick SiN_x membranes separated by ~200 nm thick spacer that sandwich the specimen solution.[54] In the case of NP encapsulation experiments, gold NPs (at a final working concentration of $\sim 3.7 \times 10^{12}$ NPs per mL polystyrene-capped gold NPs or $\sim 4.9 \times 10^{11}$ NPs per mL citrate-capped gold NPs) were added into the copolymer solution. Before loading the solution, the liquid cells were treated with

oxygen plasma to render their SiN_x membrane surfaces hydrophilic. In each case, the liquid cell was sealed inside the Liquid Flow TEM holder (Hummingbird Scientific, Lacey, WA, USA) and inserted into a JEOL 2010FEG TEM (JEOL Ltd, Akishima, Tokyo, Japan) operated at 200 kV. Note that there is ~5 min delay between the time the solution is prepared to the time it is imaged in the TEM. This delay includes the time needed to load the sample into the liquid cell holder and transfer the holder into the TEM. TEM image series of micelle formation and NP encapsulation were recorded at a rate of 10 frames per second with a OneView CMOS camera (Gatan, Inc., Pleasanton, CA, USA). *In situ* TEM imaging experiments were performed with low electron flux ranging from 1 to 4.5 e^- $(Å^2\ s)^{-1}$. Because of the low signal-to-noise ratio associated with low electron flux imaging, nine and five consecutive frames of the recorded image sequence files were summed for each image frame (moving average) displayed in the manuscript and the ESI videos,† respectively.

Molecular dynamics simulations

Encapsulated Gold NP and micelles were modeled using atomistic MD simulations. Gold NP with a diameter of 5.2 nm was covered by 60 –SH terminated and 3.01 nm long polystyrene ($(C_8H_8)_{11}$) molecules. Here, in order to reduce the computation time, we simulated the encapsulation of the NP that is smaller (5.2 nm) than the NPs (~15 nm) used in our experiments. The encapsulation process should depend little on the NP size, and the only difference might be a slightly smaller curvature of the larger NPs. However, we do not anticipate that the block copolymer shell would self-assemble differently around the larger NP. Micelles were formed through the aggregation of amphiphilic triblock copolymers (EO_{100}-PO_{65}-EO_{100}). All systems were simulated in TIP3 water. The MD simulations were performed with the Nanoscale Molecular Dynamics (NAMD) software package[55] for an isothermal-isobaric (NPT) ensemble at T = 300 K, using the Langevin dynamics with a damping constant of γ_{Lang} = 0.1 ps^{-1} and a time step of 2 fs for 20 ns. The CHARMM general force field[56,57] was implemented for the bond, angle, and dihedral parameters of the ligands and solvent molecules. The van der Waals (vdW) attraction and a steric repulsion, which are part of nonbonding interactions between the molecules, were described by the Lennard-Jones (LJ) potential with parameters provided by the CHARMM force field:

$$U_{LJ} = \varepsilon\left[\left(\frac{r_{min}}{r}\right)^{12} - 2\left(\frac{r_{min}}{r}\right)^{6}\right].$$

Here, r^6 and r^{12} terms describe the vdW attraction and an atomic repulsion because of overlapping electron orbitals. r_{min} is a distance where U_{LJ} (r_{min}) has a local minimum, and ε is the (negative) energy at this minimum. Nonbonding interactions were calculated using a cut-off distance of 10 Å, and long-range electrostatic interactions were calculated using the PME method[58] in the presence of periodic boundary conditions.

Conflicts of interest

The authors declare no competing financial interest.

Acknowledgements

This work was supported by the Academic Research Fund Tier 2 from Singapore Ministry of Education (MOE2016-T2-2-009) and the Singapore National Research Foundation's Competitive Research Program funding (NRF-CRP16-2015-05). P.K. acknowledges the support of the NSF-DMR grant 1506886, and C.L. acknowledges the support of the China Scholarship Council (CSC No. 201706740010) and the National Natural Science Foundation of China (No. 21875066).

References

1 X. Zhao, F. Pan, H. Xu, M. Yaseen, H. Shan, C. A. Hauser, S. Zhang and J. R. Lu, *Chem. Soc. Rev.*, 2010, **39**, 3480–3498.
2 T. Shimizu, M. Masuda and H. Minamikawa, *Chem. Rev.*, 2005, **105**, 1401–1444.
3 P. Alexandridis, *Curr. Opin. Colloid Interface Sci.*, 1996, **1**, 490–501.
4 S. J. Singer and G. L. Nicolson, *Science*, 1972, **175**, 720–731.
5 R. Dawson, *Biol. Rev.*, 1957, **32**, 188–229.
6 B. Dubertret, P. Skourides, D. J. Norris, V. Noireaux, A. H. Brivanlou and A. Libchaber, *Science*, 2002, **298**, 1759–1762.
7 Z. Chen, J. Wang, W. Sun, E. Archibong, A. R. Kahkoska, X. Zhang, Y. Lu, F. S. Ligler, J. B. Buse and Z. Gu, *Nat. Chem. Biol.*, 2018, **14**, 86–93.
8 K. Kataoka, A. Harada and Y. Nagasaki, *Adv. Drug Delivery Rev.*, 2001, **47**, 113–131.
9 B. Jeong, Y. H. Bae, D. S. Lee and S. W. Kim, *Nature*, 1997, **388**, 860.
10 R. M. Choueiri, E. Galati, H. Therien-Aubin, A. Klinkova, E. M. Larin, A. Querejeta-Fernandez, L. Han, H. L. Xin, O. Gang, E. B. Zhulina, M. Rubinstein and E. Kumacheva, *Nature*, 2016, **538**, 79–83.
11 D. Zhao, Q. Huo, J. Feng, B. F. Chmelka and G. D. Stucky, *J. Am. Chem. Soc.*, 1998, **120**, 6024–6036.
12 M. Goren and R. B. Lennox, *Nano Lett.*, 2001, **1**, 735–738.
13 C. Boucher-Jacobs, M. Rabnawaz, J. S. Katz, R. Even and D. Guironnet, *Nat. Commun.*, 2018, **9**, 841.
14 M. V. Seregina, L. M. Bronstein, O. A. Platonova, D. M. Chernyshov, P. M. Valetsky, J. Hartmann, E. Wenz and M. Antonietti, *Chem. Mater.*, 1997, **9**, 923–931.
15 S. Förster and M. Antonietti, *Adv. Mater.*, 1998, **10**, 195–217.
16 Y. Mai and A. Eisenberg, *Chem. Soc. Rev.*, 2012, **41**, 5969–5985.
17 A. Halperin, *Macromolecules*, 1987, **20**, 2943–2946.
18 S. A. Jenekhe and X. L. Chen, *Science*, 1998, **279**, 1903–1907.

19 Y. Shibasaki, B.-S. Kim, A. J. Young, A. L. McLoon, S. C. Ekker and T. A. Taton, *J. Mater. Chem.*, 2009, **19**, 6324–6327.
20 X. Michalet, F. Pinaud, L. Bentolila, J. Tsay, S. Doose, J. Li, G. Sundaresan, A. Wu, S. Gambhir and S. Weiss, *science*, 2005, **307**, 538–544.
21 X. Gao, Y. Cui, R. M. Levenson, L. W. Chung and S. Nie, *Nat. Biotechnol.*, 2004, **22**, 969.
22 J. Nicolas, S. Mura, D. Brambilla, N. Mackiewicz and P. Couvreur, *Chem. Soc. Rev.*, 2013, **42**, 1147–1235.
23 M. Elsabahy and K. L. Wooley, *Chem. Soc. Rev.*, 2012, **41**, 2545–2561.
24 J. P. Blitz, J. L. Fulton and R. D. Smith, *J. Phys. Chem.*, 1988, **92**, 2707–2710.
25 X. Wang, G. Guerin, H. Wang, Y. Wang, I. Manners and M. A. Winnik, *Science*, 2007, **317**, 644–647.
26 M. Wolff, U. Scholz, R. Hock, A. Magerl, V. Leiner and H. Zabel, *Phys. Rev. Lett.*, 2004, **92**, 255501.
27 S. H. Chen, *Annu. Rev. Phys. Chem.*, 1986, **37**, 351–399.
28 I. Goldmints, F. K. von Gottberg, K. A. Smith and T. A. Hatton, *Langmuir*, 1997, **13**, 3659–3664.
29 S. Couderc, Y. Li, D. M. Bloor, J. F. Holzwarth and E. Wyn-Jones, *Langmuir*, 2001, **17**, 4818–4824.
30 P. Alexandridis and J. F. Holzwarth, *Langmuir*, 1997, **13**, 6074–6082.
31 F. M. Ross, *Science*, 2015, **350**, 1490.
32 M. J. Williamson, R. M. Tromp, P. M. Vereecken, R. Hull and F. M. Ross, *Nat. Mater.*, 2003, **2**, 532.
33 H. Zheng, S. A. Claridge, A. M. Minor, A. Paul Alivisatos and A. U. Dahmen, *Nano Lett.*, 2009, **9**, 2460–2465.
34 H. Zheng, R. K. Smith, Y.-w. Jun, C. Kisielowski, U. Dahmen and A. P. Alivisatos, *Science*, 2009, **324**, 1309–1312.
35 N. D. Loh, S. Sen, M. Bosman, S. F. Tan, J. Zhong, C. A. Nijhuis, P. Král, P. Matsudaira and U. Mirsaidov, *Nat. Chem.*, 2016, **9**, 77.
36 B. Luo, J. W. Smith, Z. Ou and Q. Chen, *Acc. Chem. Res.*, 2017, **50**, 1125–1133.
37 S. F. Tan, S. W. Chee, G. Lin and U. Mirsaidov, *Acc. Chem. Res.*, 2017, **50**, 1303–1312.
38 N. K. Hima, W. Huan and G. Steve, *Adv. Mater.*, 2017, **29**, 1703555.
39 L. R. Parent, E. Bakalis, A. Ramirez-Hernandez, J. K. Kammeyer, C. Park, J. de Pablo, F. Zerbetto, J. P. Patterson and N. C. Gianneschi, *J. Am. Chem. Soc.*, 2017, **139**, 17140–17151.
40 M. A. Touve, C. A. Figg, D. B. Wright, C. Park, J. Cantlon, B. S. Sumerlin and N. C. Gianneschi, *ACS Cent. Sci.*, 2018, **4**, 543–547.
41 J.-J. Lin, J.-S. Chen, S.-J. Huang, J.-H. Ko, Y.-M. Wang, T.-L. Chen and L.-F. Wang, *Biomaterials*, 2009, **30**, 5114–5124.
42 R. Mondal, N. Ghosh and S. Mukherjee, *J. Phys. Chem. B*, 2016, **120**, 2968–2976.
43 P. Alexandridis, J. F. Holzwarth and T. A. Hatton, *Macromolecules*, 1994, **27**, 2414–2425.
44 S. Sen, Y. Han, P. Rehak, L. Vuković and P. Král, *Chem. Soc. Rev.*, 2018, **47**, 3849–3860.
45 T. Nicolai, O. Colombani and C. Chassenieux, *Soft Matter*, 2010, **6**, 3111.
46 A. G. Denkova, E. Mendes and M.-O. Coppens, *Soft Matter*, 2010, **6**, 2351.
47 E. G. Kelley, R. P. Murphy, J. E. Seppala, T. P. Smart, S. D. Hann, M. O. Sullivan and T. H. Epps, *Nat. Commun.*, 2014, **5**, 3599.
48 J. van Stam, S. Creutz, F. C. De Schryver and R. Jérôme, *Macromolecules*, 2000, **33**, 6388–6395.
49 Y. Wang, R. Balaji, R. P. Quirk and W. L. Mattice, *Polym. Bull.*, 1992, **28**, 333–338.
50 B. K. Johnson and R. K. Prud'homme, *Phys. Rev. Lett.*, 2003, **91**, 118302.
51 R. Zana, C. Marques and A. Johner, *Adv. Colloid Interface Sci.*, 2006, **123–126**, 345–351.
52 G. S. Kwon and K. Kataoka, *Adv. Drug Delivery Rev.*, 1995, **16**, 295–309.
53 L. Vuković, A. Madriaga, A. Kuzmis, A. Banerjee, A. Tang, K. Tao, N. Shah, P. Král and H. Onyuksel, *Langmuir*, 2013, **29**, 15747–15754.
54 G. Lin, S. W. Chee, S. Raj, P. Král and U. Mirsaidov, *ACS Nano*, 2016, **10**, 7443–7450.
55 J. C. Phillips, R. Braun, W. Wang, J. Gumbart, E. Tajkhorshid, E. Villa, C. Chipot, R. D. Skeel, L. Kalé and K. Schulten, *J. Comput. Chem.*, 2005, **26**, 1781–1802.
56 K. Vanommeslaeghe, E. Hatcher, C. Acharya, S. Kundu, S. Zhong, J. Shim, E. Darian, O. Guvench, P. Lopes, I. Vorobyov and A. D. Mackerell, *J. Comput. Chem.*, 2010, **31**, 671–690.
57 W. Yu, X. He, K. Vanommeslaeghe and A. D. MacKerell, *J. Comput. Chem.*, 2012, **33**, 2451–2468.
58 T. Darden, D. York and L. Pedersen, *J. Chem. Phys.*, 1993, **98**, 10089–10092.